Electron transport in unipolar InGaN/GaN multiple quantum well structures grown by NH_3 molecular beam epitaxy

David A. Browne, Baishakhi Mazumder, Yuh-Renn Wu, and James S. Speck

Citation: Journal of Applied Physics **117**, 185703 (2015); doi: 10.1063/1.4919750
View online: https://doi.org/10.1063/1.4919750
View Table of Contents: http://aip.scitation.org/toc/jap/117/18
Published by the American Institute of Physics

Electron transport in unipolar InGaN/GaN multiple quantum well structures grown by NH_3 molecular beam epitaxy

David A. Browne,[1] Baishakhi Mazumder,[1,2] Yuh-Renn Wu,[3] and James S. Speck[1]
[1]*Materials Department, University of California, Santa Barbara, California 93106, USA*
[2]*Center for Nanophase and Materials Sciences, Oak Ridge National Laboratory, Oak Ridge, Tennessee 37831, USA*
[3]*Graduate Institute of Photonics and Optoelectronics and Department of Electrical Engineering, National Taiwan University, Taipei, Taiwan*

(Received 4 December 2014; accepted 23 April 2015; published online 8 May 2015)

Unipolar-light emitting diode like structures were grown by NH_3 molecular beam epitaxy on c plane (0001) GaN on sapphire templates. Studies were performed to experimentally examine the effect of random alloy fluctuations on electron transport through quantum well active regions. These unipolar structures served as a test vehicle to test our 2D model of the effect of compositional fluctuations on polarization-induced barriers. Variables that were systematically studied included varying quantum well number from 0 to 5, well thickness of 1.5 nm, 3 nm, and 4.5 nm, and well compositions of $In_{0.14}Ga_{0.86}N$ and $In_{0.19}Ga_{0.81}N$. Diode-like current voltage behavior was clearly observed due to the polarization-induced conduction band barrier in the quantum well region. Increasing quantum well width and number were shown to have a significant impact on increasing the turn-on voltage of each device. Temperature dependent IV measurements clearly revealed the dominant effect of thermionic behavior for temperatures from room temperature and above. Atom probe tomography was used to directly analyze parameters of the alloy fluctuations in the quantum wells including amplitude and length scale of compositional variation. A drift diffusion Schrödinger Poisson method accounting for two dimensional indium fluctuations (both in the growth direction and within the wells) was used to correctly model the turn-on voltages of the devices as compared to traditional 1D simulation models. © *2015 AIP Publishing LLC*.
[http://dx.doi.org/10.1063/1.4919750]

I. INTRODUCTION

Indium gallium nitride (InGaN) based multi quantum well structures are the prominent active region design for high efficiency light emitting diodes (LEDs) and laser diodes (LDs) for solid state lighting and high efficiency blue and green lasers.[1,2] Despite a variety of difficulties including high threading dislocation densities due to growth on foreign substrates, large polarization-related electric fields, and very low temperatures required for InGaN growth, remarkable progress has been made.[3,4] Due to the presence of such large electric fields, a variety of active region designs have been proposed to maximize the electron and hole wavefunction overlap and thus reduce the deleterious quantum-confined Stark effect (QCSE).[5] The advent of multi quantum well designs has greatly improved device performance, however further advances have been hindered due to a poor understanding of carrier transport through these complex active regions.

Many previous studies addressing carrier transport have assumed equal spreading of carriers throughout many wells in active regions, however later experiments demonstrated that only a fraction of wells actually contribute to light output.[6,7] Explicit calculations of carrier injection through these structures require the Boltzmann transport equations, calculation of electron and hole wavefunctions, as well as accurate drift-diffusion and tunneling calculations. Solutions to the Schrödinger, Poisson, and transport equations become exceedingly difficult as injection increases in which drift-diffusion models have been shown to incorrectly predict device behavior. Typical simulation software using these models[8,9] has consistently overestimated the turn-on voltage for LEDs. A variety of reasons to explain this discrepancy have been proposed, however nearly all assume an abrupt interface and uniform alloy composition in the quantum wells. Other studies have investigated the transport behavior of triangular and parabolic quantum well compositional profiles.[10] Atom probe tomography (APT) measurements have shown the universal presence of indium compositional fluctuations within the InGaN alloy, which follow a random binomial distribution.[11–13] 2D calculations have demonstrated the large effect on LED device behavior by accounting for alloy fluctuations with much better agreement to experimental data than previous models.[14] By accounting for these fluctuations, the large effect on transport behavior has been identified, however the transport process within an LED active region is still complicated by fundamental differences in electron and hole transport behavior, the presence of many quantum wells, and recombination dynamics.

In this study, we have designed a series of experiments, characterization techniques, and simulations to further elucidate carrier transport through multi quantum well active regions for active regions similar to blue LEDs. Investigating unipolar structures allows us to focus solely on electron transport without radiative or nonradiative recombination with holes that complicates the understanding of carrier transport.

The transport is facilitated by drift due to applied fields rather than diffusion-based minority carrier transport in true diode active regions, however our simulations implemented a 2D drift-diffusion model. Furthermore, we restricted our analysis to correctly analyze the conduction band that is relevant for electron transport using well accepted polarization constants[15,16] and band offsets.[17] Finally, we accounted for indium fluctuations within the quantum wells with APT analysis of our sample and used the magnitude and characteristic length scale of the fluctuations to accurately interpret our experimental transport measurements.

II. EXPERIMENT

All samples in this study were grown in a Veeco Gen 930 NH_3-modified molecular beam epitaxy chamber on 1 cm $\times$ 1 cm c plane (0001) 3 μm thick MOCVD-grown GaN on sapphire templates acquired from Lumilog with dislocation densities specified as $\sim 5 \times 10^8$ cm^{-2}. High purity group III elements were provided during growth via dual filament effusion cells with calibrated fluxes measured by an ion gauge directed to the growth position. High purity ammonia was provided during growth using a showerhead injector directed at the substrate where it was thermally decomposed by the substrate heater to provide active nitrogen species for growth. The growth structure for all series consisted of a 300 nm Si doped bottom contact layer at [Si] 5×10^{18} cm^{-3} followed by an undoped active region of InGaN wells and GaN barriers and finally a 300 nm n type top contact layer also doped at 5×10^{18} cm^{-3}. From previous measurements, we estimate an unintentional donor (UID) concentration of 1×10^{16} cm^{-3} for UID GaN and 5×10^{16} cm^{-3} for the UID InGaN. Growth rates and compositions were determined using calibration samples analyzed by triple axis High Resolution X-ray Diffraction (HRXRD) prior to device growth. The InGaN composition was controlled by reducing the substrate temperature during growth to realize the target indium composition in the InGaN layers. The silicon concentration was calibrated using SIMS analysis by Evans Analytic Group (Sunnyvale, CA). Substrate temperature was measured using an infrared pyrometer calibrated to the melting point of aluminum.

Growth rates and ammonia flow rates of 400 nm/h at 200 sccm and 80 nm/h at 500 sccm were used for GaN and InGaN layers, respectively. InGaN quantum well growth consisted of a growth interruption to reduce the substrate temperature with suitably long pause, typically 5–10 min, to stabilize the growth temperature. Substrate temperatures of 575 °C and 590 °C were used to grow quantum wells with compositions of 19% and 13%–14%, resulting in photoluminescence at 470 nm and 440 nm, respectively. Upon completion of well growth, a 2 nm low temperature GaN barrier was grown as the temperature was increased to the standard GaN growth temperature of 830 °C. A subsequent growth interruption was then included to stabilize the temperature prior to the next well growth.[18]

All samples were processed for electrical testing using a two-step contact photolithography process. Reactive ion etching using a 100W BCl_3/Cl_2 process was used to define mesas followed by a second lithography to define areas for metallization. Ohmic contacts were formed using an unannealed Al (30 nm)/Au (300 nm) stack. A cross sectional view of a general device structure is shown in Fig. 1.

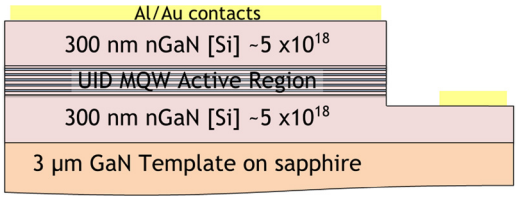

FIG. 1. Cross sectional schematic showing the standard device structure after processing to 100 μm mesas.

For all samples, the total thickness of the UID "active region" was fixed at 63 nm, such that even for varying the quantum well number or thickness, the total UID thickness remained constant. A range of mesa sizes were fabricated on each sample but no large deviations were observed for devices of different sizes. All data reported will be for 100 μm $\times$ 100 μm square mesa devices. Temperature dependent current-voltage measurements were performed in a vacuum probe station with a Hewlett Packard 4155B semiconductor parameter analyzer. APT measurements were performed using a Cameca Instruments Local Electrode Atom Probe (LEAP) 3000X HR. The needle shape specimens were prepared using a Focused Ion Beam (FIB) liftout technique. The quantum well region of interest was protected from Ga ion damage in FIB with an electron beam deposited Ni layer on the top nGaN layer. The samples were then analyzed at 30 K with a laser pulse energy of 0.1 nJ, a pulse frequency of 200 kHz, and a detection rate of 1%. Accurate alloy composition is reported using only the ratio of Group III In/(Ga + In) atoms to avoid the selective efficiency differences of the ion detector to N atoms, as has been shown elsewhere.[19] Temperature dependent IV measurements were performed under vacuum using a Joule Thompson-cooled refrigerator with a heated stage from MMR Technologies.

1D simulations of band diagrams were generated using commercially available SiLENSe software from STR Inc. This software is intended to be used for the modeling of LED heterostructures as a function of applied bias, carrier transport, and recombination dynamics by implementing a 1D drift diffusion model. 1D simulations of current-voltage behavior were performed by computing electron and hole currents as a function of applied bias. This software fully accounts for electrons and holes, however for our structures we only needed to consider electron behavior, as for all biases the hole quasi-Fermi level was at least 2.5 eV above the valence band maximum. We will subsequently refer to all SiLENSe band diagrams and current voltage characteristics as 1D simulations. 2D simulations of current voltage behavior were performed using a modified drift diffusion model that accounted for lateral indium fluctuations within each quantum well. Compositional parameters were obtained from APT measurements of devices, using a sinusoidal lateral fluctuation model and employing a Gaussian shape to describe the well profile in the growth direction. Further details of the 2D simulations are addressed in the Results and Discussion section.

III. RESULTS AND DISCUSSION

A. Quantum well depth and number

Analysis of the effect on vertical transport of both the quantum well depth and number is presented in this section. The quantum well depth was controlled by indium composition which also affects the polarization-induced barrier height. The compressive strain causes a larger piezoelectric component to the polarization-related electric field in the quantum well which has been shown to significantly affect carrier transport.[20] We define the turn-on of the device in forward bias at 20 A/cm^2 which is a relevant current density regime for LED operation. Forward bias refers to a positive bias on the free surface while the bottom contact is grounded, in the same orientation as defined for typical LED testing. This convention to describe device turn-on is used for the remainder of the paper.

The simulated unbiased 1D band diagrams using SiLENSe are presented in Fig. 2(a) for single 3 nm quantum wells with indium compositions of 13% and 19%. It was evident that the largest effect of the higher indium composition is the conduction band barrier being ~0.2 eV higher for the 19% sample when compared to the 13% sample. Figure 2(b) presents the experimental and 1D simulated JV curves for forward bias with single quantum wells of both compositions. Despite the expected presence of this barrier, the experimental JV characteristics of the devices in Fig. 2(b) showed substantial current at low bias instead of any clear turn-on as in 1D simulations. For all applied biases, the experimentally measured current for the 19% InGaN well sample was lower than the 13% InGaN well sample; however, both were significantly higher current than 1D simulations for a barrier height of that size. The measured turn-on voltage at 20 A/cm^2 of the devices was 0.085 V and 0.131 V for the 13% and 19% samples, respectively. The physical basis for explaining the observed early device turn-on is addressed using a using the indium fluctuation model developed later in this paper.

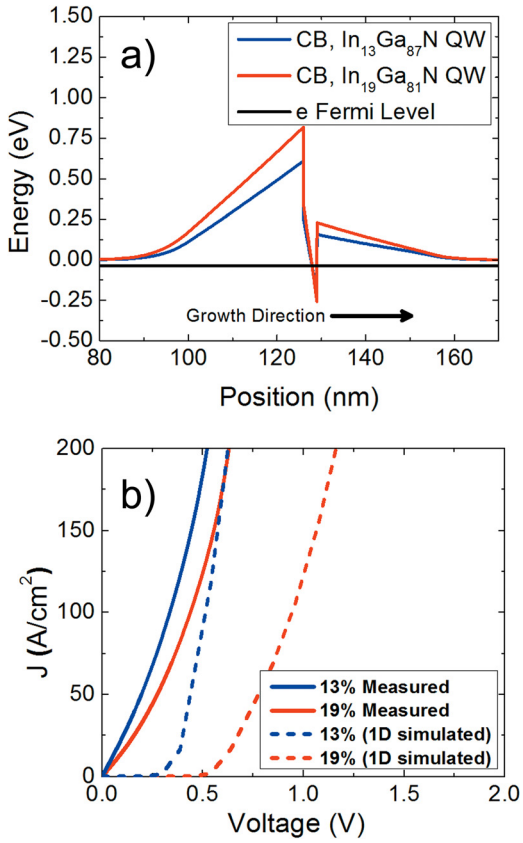

FIG. 2. (a) Simulated zero bias 1D SiLENSe conduction band diagrams for single 3 nm thick quantum well structures of 13% and 19% indium composition. (b) Experimental and 1D SiLENSe simulated JV characteristics for SQW structures; solid lines represent experimental data and dashed lines represent 1D simulated data.

Additionally, the effect of quantum well number was investigated. Figure 3 shows the JV characteristic of samples that included 0, 1, and 5 wells. The "0 well" sample was included in the series with the same total UID thickness but no quantum wells and was processed at the same time such that the total resistance of rest of the structure could be measured. Typical contact resistances were measured to be ~4 $\times 10^{-4}$ Ω cm^2 and ~2 $\times 10^{-4}$ Ω cm^2 for top and bottom contacts, respectively. It was found that the contact resistance dominated this resistance as the bulk resistance of the n-GaN and UID GaN layers was small. We observed asymmetry of the JV characteristics in all samples for forward and reverse bias which was expected due to the effect of the polarization induced electrics fields. In forward bias, the triangular nature of the quantum barriers was flattened, while in reverse they became steeper. This leads to a lower turn-on in forward bias because of a voltage induced lowering of barrier height. In reverse bias, the turn-on occurs at a greater voltage as the barriers become larger but also steeper. This steepening leads to an effective narrowing of barrier thickness which likely allows a larger component of carrier tunneling. We focus our analysis on the forward voltage regime for the remainder of this paper, as this is the relevant voltage sense for LED operation. For the 5 QW samples, the turn-on voltages were much higher than for the single QW samples. Despite the same thickness of UID active region, the applied voltage is dropped across multiple barriers for the 5 QW sample, requiring larger total applied bias for device turn-on. An increased turn-on voltage was observed for the 19% InGaN quantum well samples as expected with increasing barrier height. This effect of InGaN composition was much more

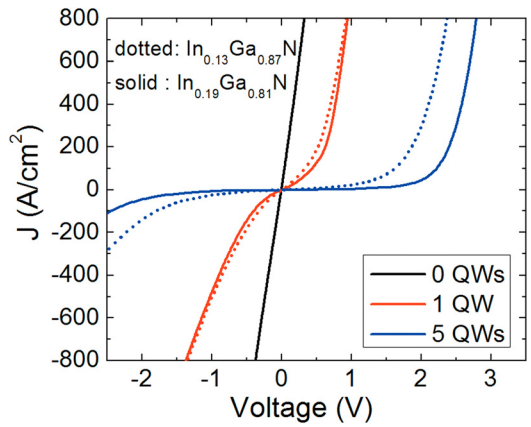

FIG. 3. Experimental JV curves for processed devices varying quantum well number and composition for 3 nm thick quantum wells. Dotted lines represent 13% In quantum wells and solid lines represent 19%.

evident in the 5 QW samples compared to the small difference in the single QW samples.

B. Quantum well width

The effect of varying quantum well width was also investigated using similar 5 QW structures where quantum well widths of 1.5, 3.0, and 4.5 nm were chosen. Varying the quantum well width changes both the bound state of the electron energy level within the well and the conduction band barrier height due to the very large internal polarization-related electric fields, as shown in the simulated band diagram of Fig. 4.

Quantum well width is typically experimentally optimized for device performance depending on substrate orientation and thus field strength within the wells. This is due to a number of factors including intended operating current densities, quantum well number, and inability to accurately predict device performance *a priori* such that explicit experimental optimization is required. Additionally, long wavelength devices require high indium composition and therefore highly strained wells which preclude the use of thick wells. Quantum well widths and compositions were chosen for this series such that we assume negligible stress relaxation has occurred and that the quantum wells are all fully strained and coherent. Again, a 0 QW control sample was included in the quantum well width sample series which was used to determine bulk resistances and contact resistances. Varying the quantum well width and therefore changing barrier height has a direct impact on the electrical transport behavior as is evident in Fig. 5.

With increasing quantum well width, the barrier height increased and a higher voltage was necessary for significant current flow. The turn-on of the devices was 0.08 V, 0.79 V, and 2.11 V for quantum well thicknesses of 1.5 nm, 3.0 nm, and 4.5 nm, respectively. After device turn-on, the transport in the series resistance-limited regime matched that of the 0 QW control sample, such that all samples have similar dynamic resistances. Therefore, we attributed the turn-on behavior of the device solely to the lowering of the barriers with applied forward bias in the active regions in each sample. Figure 5 shows the forward bias regime where the experimental data exhibits turn-on at much lower voltages than calculated by the 1D SiLENSe model. The turn-on of the SiLENSe calculations was about one volt higher for all samples, which was less than the overestimation observed in LED comparisons.[12] In these unipolar structures, no built in electric field exists as in a diode. Therefore, the only barrier to carrier transport that exists is due to the presence of the strong polarization related electric fields in the quantum barriers of the active region.

With increasing forward bias, the effective barrier height is lowered as shown in Fig. 6. Simulated 1D room temperature band diagrams are presented at the respective voltages required for a current density of 200 A/cm^2. Larger voltages are required with increasing quantum well thickness and effective barrier height as observed experimentally. While these voltages were higher than those observed in experiment, the figure serves as a representation of the band structure under bias. The initial barrier to electron transport must be lowered to a comparable level for equal current to flow. At this point, the barrier is sufficiently low for significant current to flow through the active region despite the different subsequent heights of the quantum barriers.

We next performed temperature dependent IV measurements to further elucidate relevant transport mechanisms governing device performance. Previous speculation of the mechanism of early experimental turn-on compared to calculations has suggested threading dislocation mediated leakage, defect, or impurity related tunneling, electron overflow due to incomplete capture in quantum wells, or indium

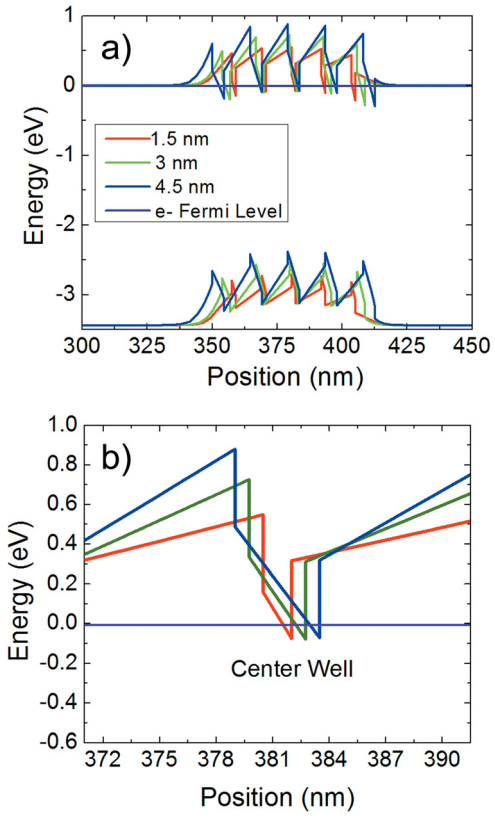

FIG. 4. (a) 1D SiLENSe simulated conduction band diagrams for 5 quantum well samples varying the quantum well width. (b) View of conduction band profile for all samples in the region of the central quantum well.

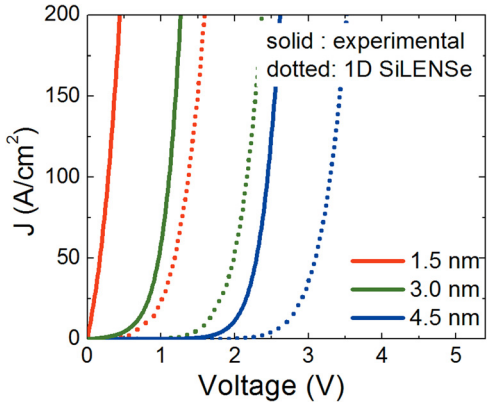

FIG. 5. Forward bias JV characteristics for quantum well width series forward bias regime with experimental data (solid) and 1D SiLENSe simulated data (dotted).

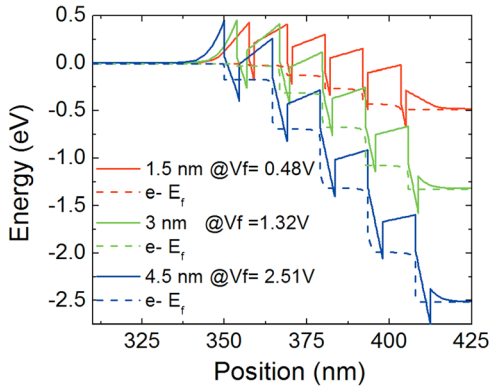

FIG. 6. 1D SiLENSe simulated conduction band profiles for 5× quantum well width series at equal current density (200 A/cm^2) under forward bias. The dotted lines denote respective electron Fermi levels.

fluctuations.[9] Threading dislocation leakage is not likely to be the dominant mechanism as dislocations would act as a parallel current pathway and shunt the device. Thus, a clear turn on would not be observed if a significant parallel current pathway was present. We cannot comment on electron overflow for these structures since no holes are present, and all current could be considered overflow by the traditional definition, therefore it is not relevant. The relative influence of the remaining two mechanisms was elucidated by temperature dependent transport measurements. Transport in unipolar structures with heterojunction barriers should be limited by either thermionic emission current or tunneling current depending on barrier heights and thicknesses; however, it is likely that contributions exist from both mechanisms. A strong temperature dependence on device turn-on would indicate thermionic limited behavior, while tunneling processes are much more insensitive to temperature. Figure 7 shows the JV curves for all three samples from low temperature to 400 K.

All devices exhibited a strong temperature dependence thus clearly indicating the presence of a thermally activated transport process. With increasing temperature, the turn-on voltage was systematically decreased in a clear and repeatable manner. The reduction in turn-on voltage is expected due to the occupation of higher energy electrons states from thermal energy. For the 1.5 nm well sample, linear JV behavior was observed upon heating to 400 K. The linear JV behavior of the thin quantum wells at 400 K is inconsistent with the simulated 1D band diagrams which predict a barrier height of ~0.4 eV as seen in Fig. 4. This is much greater than the expected thermal energy for electrons at this temperature of ~35 meV. This temperature dependent behavior supported the presence of a significantly smaller barrier height which we attribute to compositional fluctuations within the wells. Therefore, at 400 K, electrons are able to easily transport throughout the entire active region despite the predicted barriers, and the structure shows ohmic behavior.

The dominant current transport mechanism based on the temperature dependent measurements was assumed to be thermionic emission. To extract an effective barrier height from the experimental data for these active regions that

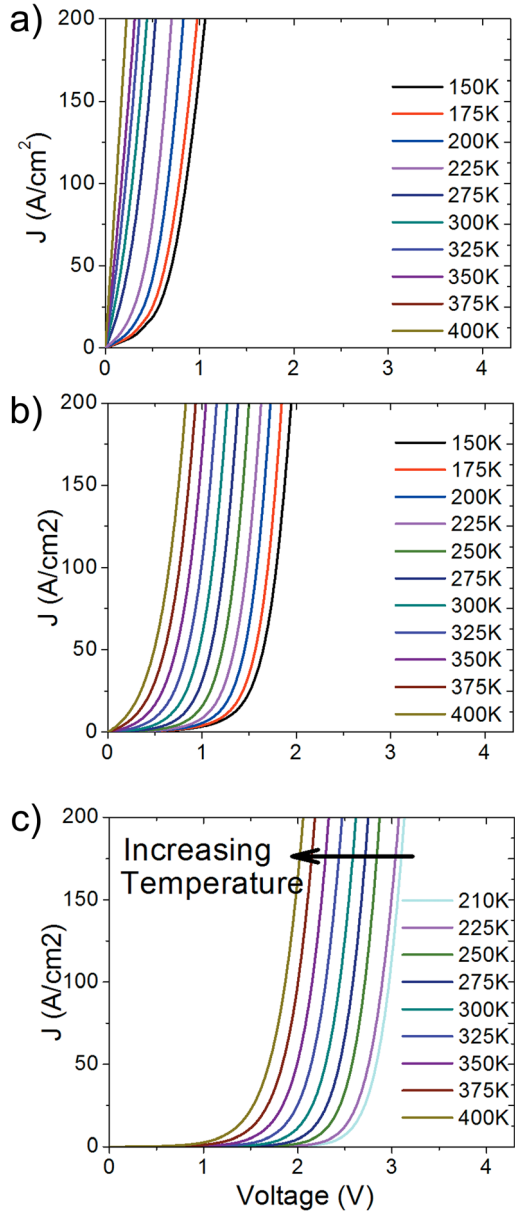

FIG. 7. Temperature dependent experimental JV curves for quantum well width series (a) 5 × 1.5 nm quantum wells. (b) 5 × 3.0 nm quantum wells. (c) 5 × 4.5 nm quantum wells.

consist of many layers, as well as very strong polarization-related electric fields, some approximations were required. Upon examination of the band diagram, the barrier to transport consists of multiple quantum barriers within the active region. For mathematical tractability, we make the assumption to treat our active region as a single barrier and employ a Richardson analysis[21–23] to extract the effective barrier heights using standard thermionic emission theory. We use the measured current at a low forward bias of 10 mV as has been done elsewhere to calculate the near flat-band barrier height.[22] Implicit in this analysis is a few additional assumptions that should be directly addressed. This analysis neglects any contribution of tunneling current which is inevitably present in our devices. The triangular barrier shape due to the polarization-related electric fields would suggest that the necessary electron energy to surmount the barrier is indeed

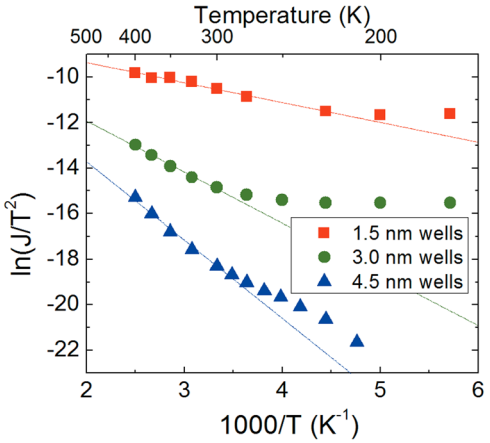

FIG. 8. Richardson plots at 10 mV forward bias for temperature dependent experimental measurements for barrier height extraction with fitted data at high temperatures.

less than the actual barrier height. Additionally, this tunneling process is thermally dependent as temperature will affect the Fermi-Dirac occupation function and allow higher energy states to be occupied at higher temperatures

$$J_{TE} = A^* \cdot T^2 \exp\left(-\frac{\phi}{kT}\right), \quad A^* = \frac{4\pi \cdot q \cdot m_e^* \cdot k^2}{h^3}. \quad (1)$$

Richardson plots of our data ($\ln(J/T^2)$ vs $1/T$) were expected to show linear behavior with the y intercept $\ln(A^*)$ and slope is $(-\phi/k)$. Figure 8 shows the data plotted in this manner where we observed two distinct regimes. At temperatures greater than room temperature, the thermionic model applied where we can extract a barrier height and intercept; however, at low temperatures larger currents were observed than predicted for pure thermionic behavior. The transition to thermally activate current around room temperature and above is in agreement to a previous LED transport study;[24] however, here we do not have a recombination current due to the absence of holes. Fitting the high temperature data in Fig. 8 showed very good agreement to the thermionic model allowing us to extract an effective barrier height. The extracted barrier heights were 0.075, 0.194, and 0.297 eV for the 1.5, 3.0, and 4.5 nm quantum well thickness samples, respectively. Comparison to the 1D simulated band diagrams in Fig. 5 showed these extracted barrier heights to be significantly less than the barrier height in the 1D SiLENSe band diagrams. Clearly, the true nature of the transport through a region with multiple quantum wells is not a simple barrier; however, these extracted values were well below even the first barrier height from a 1D model. Therefore, this analysis served as confirmation of the lower effective barrier height experienced by electrons in the thermionic temperature range and at low forward bias.

C. Atom probe tomography analysis

APT analysis was performed on the 5 QW 3.0 nm quantum well width sample for explicit investigation of the nature of indium fluctuations present in the well. Figure 9(a) shows a 3D atomic reconstruction of the analyzed volume where indium atoms are depicted in dark purple and the gallium atoms as blue dots. Five wells, each with thickness of 3 nm, are clearly distinguishable in the reconstructed volume showing very good periodicity. It was found that a random binomial distribution of atoms was observed in our sample

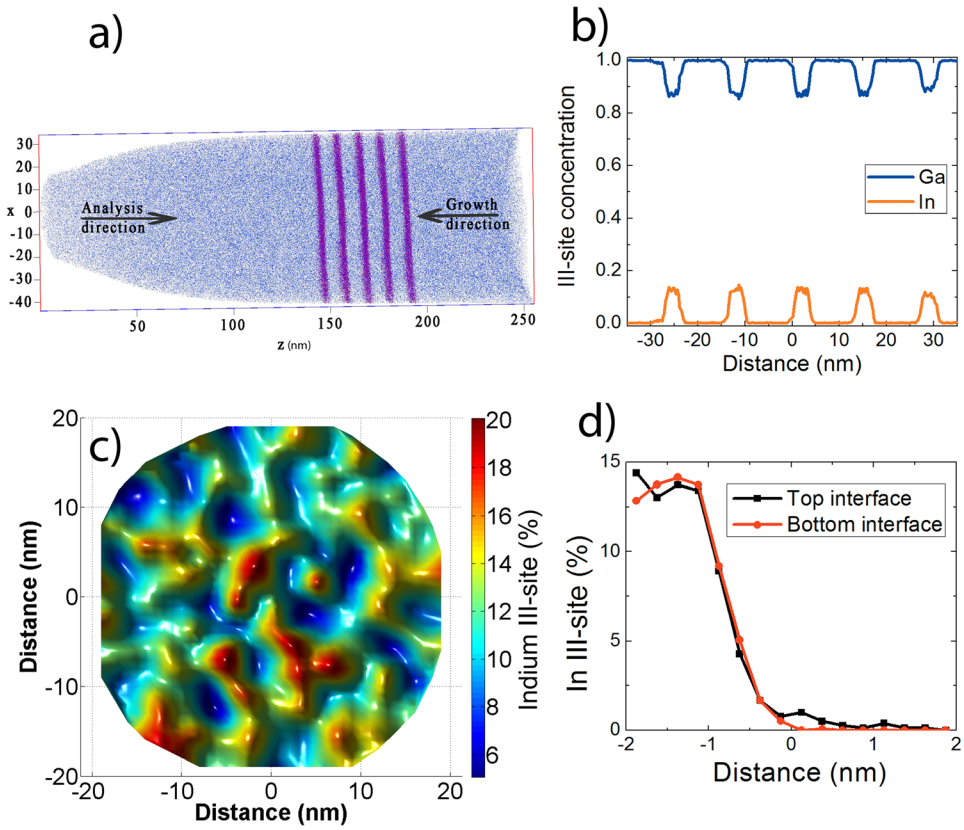

FIG. 9. Atom probe tomography analysis of the 5 × 3.0 nm quantum well sample. (a) Reconstructed view of probe tip showing the presence of the 5 QWs. (b) Line profile of group III site occupation by gallium and indium through active region. (c) 2D plot of the lateral indium composition within the central well. (d) Overlayed profile of top and bottom interfaces for the central quantum well.

which is consistent with other InGaN grown by MOCVD and measured by our group and others.[25–27] A 1D line profile is shown in Fig. 9(b) showing the uniformity of the composition and thickness for all wells. The average In III-site composition of these wells was verified to be 14%, in excellent agreement with calibration samples. Figure 9(d) shows the top and bottom interfaces of the center well showing symmetric compositional profiles on both interfaces. The interface width values for the top and bottom interfaces were calculated to be 0.77 nm and 0.75 nm, respectively, when using a 90%–10% cutoff metric. This is a standard method to quantitatively report interfacial abruptness by measuring distance from 90% of the nominal composition of the alloy to 10% in the growth direction. Figure 9(c) shows the In III-site distribution in a plane perpendicular to the growth direction. The lateral compositional profile was obtained from a 20 nm radius disk taken from the central 1.5 nm of the quantum well and collapsing the data to a single contour plot. We use the center 1.5 nm of the nominally 3.0 nm quantum well to generate the plot to avoid the influence of the quantum well and barrier interface on composition. Plotting the data using a contour plot in Fig. 9(c) allows for the visualization of local compositional variations that are not apparent when viewing the data in Fig. 9(a). A significant amplitude in the compositional fluctuations was present with regions ranging from 8% to 20%. Similar profiles were found in other regions of the well and in other wells, such that this represented a typical region of the InGaN alloy. The lateral compositional fluctuations were observed to vary over length scales as small as a few nanometers in some directions. This fluctuation profile is very similar to what has been observed by InGaN quantum wells grown by MOCVD with no observable difference in the magnitude or length scale of compositional fluctuations for quantum wells of similar composition.

D. 2D simulations

2D drift diffusion simulations were performed for the forward bias current voltage behavior of the quantum well width sample series. Adding additional dimensionality in our simulations allows short length scale alloy fluctuations to be included unlike previous 1D simulations that assume a mean alloy composition and potential landscape. These calculations inherently do not include tunneling or thermally assisted tunneling. We therefore expected some discrepancies between simulations and experimental data at low temperatures where tunneling can play a more dominant role. The simulations include a Gaussian profile of well composition in the growth direction to model the shape of the quantum well/barrier interface as depicted in Fig. 9(d). A perpendicular sinusoidal compositional variation is included within each well to model the observed alloy fluctuations clearly visible in Fig. 9(c). Since the presence of indium atoms has been found to follow a random binomial distribution, the true potential landscape is extremely complex. Full 3D simulations would be more accurate in which the entire in-plane compositional profile would be inputted in the simulations, but at this time these simulations are too computationally intensive so we restricted our analysis to a one dimensional in-plane sinusoidal profile and a one dimensional out-plane Gaussian shape profile. Fixed parameters in these simulations included a mobility of 300 cm^2/V s in the n-GaN and a mobility of 600 cm^2/V s in the intrinsic region. To model the composition fluctuation in the MQW intrinsic active region, the mesh grid size is 2.0 nm in the lateral direction to represent the sinusoidal distribution, and 0.1 nm in the vertical direction in the intrinsic active region. Indium composition values were taken from the APT analysis of the 3.0 nm quantum well width sample and directly inputted into the calculations. The nature of the well profile as shown in Fig. 9(d) can be fit with a symmetric Gaussian function where the indium composition In(z) is varying at the well barrier heterointerface using

$$In(z) = \exp\left(\frac{-(z-a)^2}{\sigma^2}\right). \tag{2}$$

The Gaussian RMS width, σ, used to fit the 5 × 3.0 nm QW samples was chosen to be 1.5 nm, and the lateral indium fluctuation was modeled using a sinusoidal function shown in

$$In(x) = A \cdot \sin(\mathrm{B} \times 2\pi + \mathrm{C}) + \mathrm{H}. \tag{3}$$

The A term defines the magnitude of the fluctuations, while the B term describes the period of the fluctuations. The C term in Eq. (3) is a phase shift which staggers the fluctuations in each well so that minima are not aligned in the growth direction. The H term represents the average composition of the wells which was fixed in all cases at 14%, as verified by APT measurements.

The B term was fixed at 2.5 × 10^5 cm^{-1} which corresponded to a period of 40 nm. This period was larger than the finer length scale observed in the APT contour plot in Fig. 9(c), but was a necessary approximation since only fluctuations in a single lateral dimension were considered. The influence of the period of fluctuations is shown in Fig. 10. As the period is decreased for a 2D simulation, the result would approach that of a mean composition alloy. In full 3D simulations, the true distribution of random In atoms consists of many periods and not a single value. These simulations include the true random potential landscape and are the focus of ongoing work.

A visual representation of the influence of indium compositional fluctuations on barrier height is shown in Fig. 11. Indium fluctuations in the quantum wells result in locally varying strain profiles which directly influence the strength of the piezoelectric component of the induced electric field. Regions of low composition therefore induce lower barrier heights directly adjacent to each quantum well. The barrier heights are also reduced when using a Gaussian profile of the quantum wells instead of abrupt interfaces.

Figure 12 shows the JV plots for the 3.0 nm quantum well width sample for the experimental and simulated curves. 1D simulations using SiLENSe clearly showed the overestimation of turn-on voltage. Using the 2D model with a 8%–20% indium fluctuation range closely matched the experimental data. This fit was obtained when adding the contact resistances which were measured in the samples by

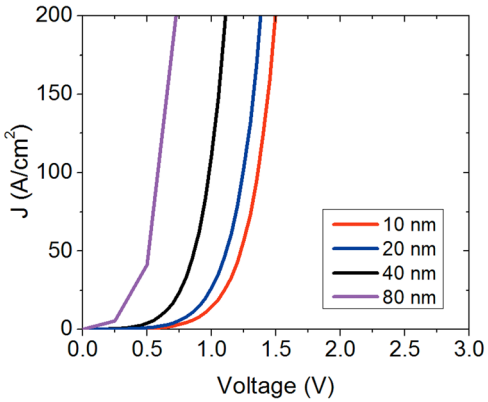

FIG. 10. The effect of changing the period of the compositional fluctuations is shown in the 2D simulations.

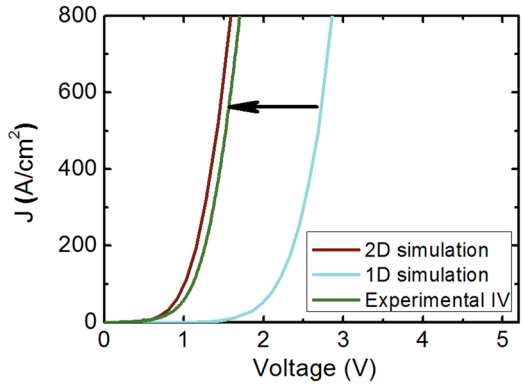

FIG. 12. Experimental and simulated JV curves for 5 × 3.0 nm quantum well sample including both 1D SiLENSe and 2D simulations.

transmission line measurements and verified by the total resistance of the control "0 QW" reference sample. It was found that the lower bound on the compositional fluctuations had a far greater impact on the nature of the simulated JV curve than the upper bound on composition. The varying indium composition causes a lateral fluctuation in barrier height to electron transport due to the changing polarization-induced barrier height that exists in the quantum barrier. Regions of low indium composition cause a lower barrier height and therefore are the regions that facilitate transport of electrons through the active region.

We then extended our calculations for the temperature range experimentally investigated for the 3.0 nm QW sample. It was necessary to account for the change in mobility in the intrinsic region as a function of temperature. We assume that phonon scattering limits the mobility so that the UID GaN mobility changes inversely as T to the 3/2 power as shown in

$$\mu_{UID} = \mu_{300\,\mathrm{K}} \times \left(\frac{300\,\mathrm{K}}{T}\right)^{3/2}. \tag{4}$$

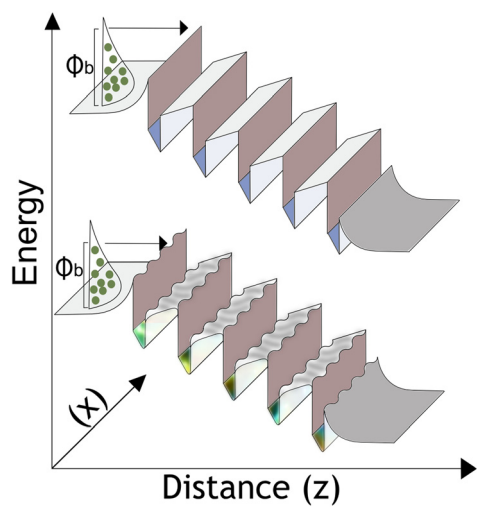

FIG. 11. Visual representation of conduction band under forward bias for isoconcentration, abrupt wells (top), and structure adding indium fluctuations in lateral direction and nonabrupt interfaces depicting lower effective barrier height (bottom). The magnitude of the barrier height fluctuations is not to scale.

Comparing the JV characteristics in Fig. 13 we found excellent agreement for high temperature data with a deviation that increased at lower temperature. At low temperature, the experimental data had significantly larger current than the 2D calculations under forward bias. It is possible that self heating of the device under large forward bias can result in higher currents; however, this cannot fully explain the observed difference. We believe this was mainly a result of a large tunneling current or a thermally assisted tunneling process. In real alloys with three dimensional alloy fluctuations, the transport process at low temperature may have a greater dependence on the thermally assisted transport nature that we cannot accurately model at this time.

After gaining sufficient confidence in our 2D simulations from modeling the 5 × 3.0 nm QW sample, we extended our analysis to the remaining samples in the quantum well width series. For the 1.5 nm quantum well width sample, all parameters inputted in the simulation were identical except changing the Gaussian width to 0.75 nm. In doing this, we were able to obtain a very good fit to match the forward bias turn-on of the experimental data. For the thickest 4.5 nm wells, we used a Gaussian width of 3.0 nm. Additionally, we found it necessary to use a compositional range of 10%–20% instead of the 8%–20% that resulted in good fits for the other samples. Our justification for changing the amplitude of the

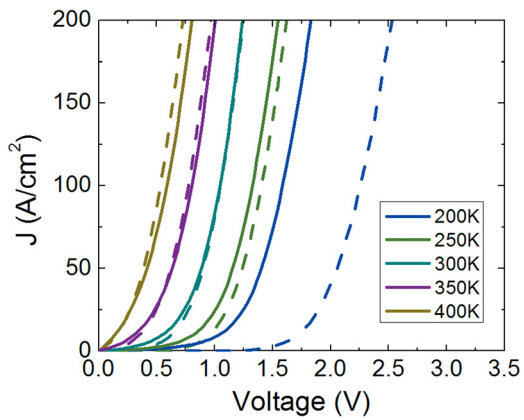

FIG. 13. Temperature dependent experimental and 2D simulations under forward bias (experimental data shown in solid, calculations shown in dashed lines).

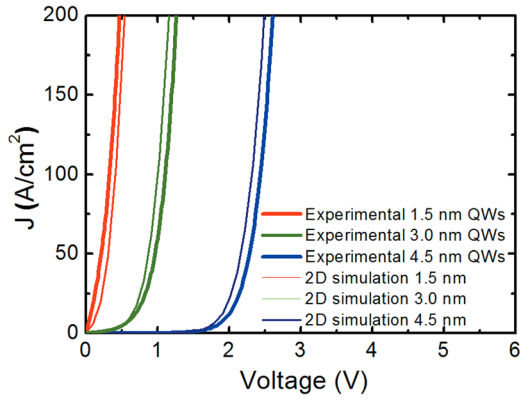

FIG. 14. Experimental and 2D simulated forward bias JV curves for all samples in 5× quantum well width series.

compositional fluctuations is as follows. With increasing alloy thickness, the likelihood of a low composition region existing throughout the entire well of the well is decreased as the real alloy has compositional fluctuations in three dimensions, whereas our calculations at the present time only consider two dimensions. Therefore, it is more appropriate to consider a lateral compositional profile which averages a greater volume. The adjacent quantum barrier experiences this electric field which is averaged due to the thicker well, and therefore has a reduced amplitude of fluctuation. The experimental and calculated currents were found to be in excellent agreement and are shown in Fig. 14.

IV. CONCLUSIONS

In this work, the vertical electron current in unipolar n-i-n InGaNGaN multi quantum well structures has been extensively studied. We have shown that the presence of indium fluctuations greatly impacted the transport behavior and caused a significant reduction of the turn-on voltage. We have used the magnitude and length scale of indium fluctuations from APT measurements of our quantum wells to accurately fit 2D Schrodinger Poisson drift diffusion calculations to our data. The effective barrier height was lowered significantly due to the presence of these natural alloy fluctuations which strongly affected the local strength of the polarization-related electric field. It was shown that the lower bound on the indium composition within the simulations greatly impacts the turn-on of these devices. We have also shown thermionic transport of electrons at temperatures above room temperature to be the dominant transport mechanism. The extracted barrier heights were consistently smaller than what was calculated using a traditional 1D band diagram model with abrupt wells of constant composition. Therefore, the lowering of the polarization-induced barrier heights must be considered in device design for accurate representation of device performance.

ACKNOWLEDGMENTS

This work was supported by funding from the Solid State Lighting Program at UCSB and from the King Abdullah University of Science and Technology and the King Abdullah Center of Science and Technology. This work made use of the Central Facilities at UCSB supported by the NSF MRSEC program. A portion of this work was done in the UCSB Nanofabrication Facility, part of the NSF-funded *National Nanotechnology Infrastructure Network*. The work in NTU was support by Ministry of Science and Technology in Taiwan for the financial support, under Grant No. MOST-102-2221-E-002-194-MY3.

[1]S. Nakamura, M. Senoh, N. Iwasa, and S. Nagahama, Jpn. J. Appl. Phys., Part 2 **34**, L797 (1995).
[2]S. Nakamura, M. Senoh, S. Nagahama, N. Iwasa, T. Yamada, T. Matsushita, H. Kiyoku, and Y. Sugimoto, Jpn. J. Appl. Phys., Part 2 **35**, L74 (1996).
[3]A. Laubsch, M. Sabathil, J. Baur, M. Peter, and B. Hahn, IEEE Trans. Electron Devices **57**, 79 (2010).
[4]Y. Narukawa, M. Ichikawa, D. Sanga, M. Sano, and T. Mukai, J. Phys. D: Appl. Phys. **43**, 354002 (2010).
[5]J. Ryou, P. D. Yoder, J. Liu, Z. Lochner, H. Kim, S. Choi, H. J. Kim, and R. D. Dupuis, IEEE J. Sel. Top. Quantum Electron. **15**, 1080 (2009).
[6]A. David, M. J. Grundmann, J. F. Kaeding, N. F. Gardner, T. G. Mihopoulos, and M. R. Krames, Appl. Phys. Lett. **92**, 053502 (2008).
[7]J. H. J. Zhu, S. M. Zhang, H. Wang, D. G. Zhao, J. H. J. Zhu, Z. S. Liu, D. S. Jiang, Y. X. Qiu, and H. Yang, J. Appl. Phys. **109**, 093117 (2011).
[8]K. A. Bulashevich, O. V. Khokhlev, I. Y. Evstratov, and S. Y. Karpov, Proc. SPIE **8278**, 827819 (2012).
[9]S. Y. Karpov, Proc. SPIE **7939**, 79391C (2011).
[10]P. M. McBride, Q. Yan, and C. G. Van de Walle, Appl. Phys. Lett. **105**, 083507 (2014).
[11]M. J. Galtrey, R. a. Oliver, M. J. Kappers, C. J. Humphreys, D. J. Stokes, P. H. Clifton, and A. Cerezo, Appl. Phys. Lett. **90**, 061903 (2007).
[12]Y.-R. Wu, R. Shivaraman, K.-C. Wang, and J. S. Speck, Appl. Phys. Lett. **101**, 083505 (2012).
[13]R. Shivaraman, Y. Kawaguchi, S. Tanaka, S. P. DenBaars, S. Nakamura, and J. S. Speck, Appl. Phys. Lett. **102**, 251104 (2013).
[14]T.-J. Yang, R. Shivaraman, J. S. Speck, and Y.-R. Wu, J. Appl. Phys. **116**, 113104 (2014).
[15]F. Bernardini, V. Fiorentini, and D. Vanderbilt, Phys. Rev. B **56**, R10024 (1997).
[16]V. Fiorentini, F. Bernardini, F. Della Sala, A. Di Carlo, and P. Lugli, Phys. Rev. B **60**, 8849 (1999).
[17]G. Martin, A. Botchkarev, A. Rockett, and H. Morkoc, Appl. Phys. Lett. **68**, 2541 (1996).
[18]S. J. Leem, Y. C. Shin, E. H. Kim, C. M. Kim, B. G. Lee, Y. Moon, I. H. Lee, and T. G. Kim, Semicond. Sci. Technol. **23**, 125039 (2008).
[19]L. Mancini, N. Amirifar, D. Shinde, I. Blum, M. Gilbert, A. Vella, W. Lefebvre, R. Larde, E. Talbot, P. Pareige, X. Portier, A. Ziani, C. Davesnne, C. Durand, J. Eymery, N. Grandjean, and L. Rigutti, J. Phys. Chem. C **118**, 24136 (2014).
[20]D. S. Sizov, R. Bhat, A. Zakharian, K. Song, D. E. Allen, S. Coleman, and C. Zah, IEEE J. Quantum Electron. **17**, 1390 (2011).
[21]S. M. Sze and K. K. Ng, *Physics of Semiconductor Devices*, 3rd ed. (John Wiley & Sons, Inc., Hoboken, NJ, 2007).
[22]A. C. Gossard, W. Brown, C. L. Allyn, and W. Wiegmann, J. Vac. Sci. Technol. **20**, 694 (1982).
[23]H. Zhao, G. Liu, J. Zhang, R. A. Arif, and N. Tansu, J. Disp. Technol. **9**, 212 (2013).
[24]I. A. Prudaev, I. Y. Golygin, S. B. Shirapov, I. S. Romanov, S. S. Khludkov, and O. P. Tolbanov, Semiconductors **47**, 1382 (2013).
[25]F. Liu, L. Huang, R. F. Davis, L. M. Porter, D. K. Schreiber, S. V. N. T. Kuchibatla, V. Shutthanandan, S. Thevuthasan, E. A. Preble, T. Paskova, and K. R. Evans, J. Vac. Sci. Technol., B **32**, 051209 (2014).
[26]T. J. Prosa, P. H. Clifton, H. Zhong, A. Tyagi, R. Shivaraman, S. P. DenBaars, S. Nakamura, and J. S. Speck, Appl. Phys. Lett. **98**, 191903 (2011).
[27]D. Watson-Parris, M. J. Godfrey, P. Dawson, R. a. Oliver, M. J. Galtrey, M. J. Kappers, and C. J. Humphreys, Phys. Rev. B **83**, 115321 (2011).